

Appendix B Burner Mechanical Drawings

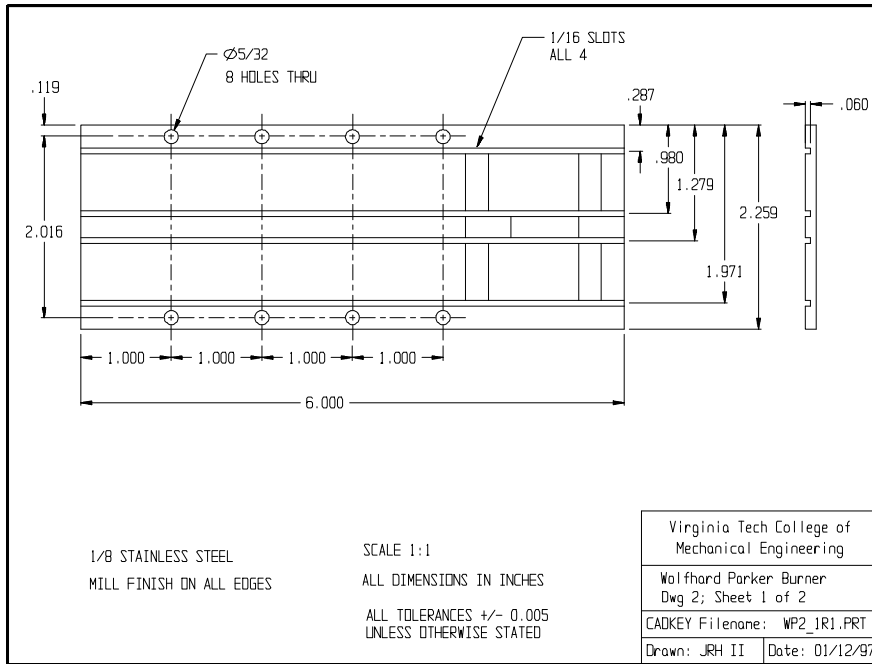


Figure B1 Burner North and South Walls, Drawing 2 Sheet 1 of 2

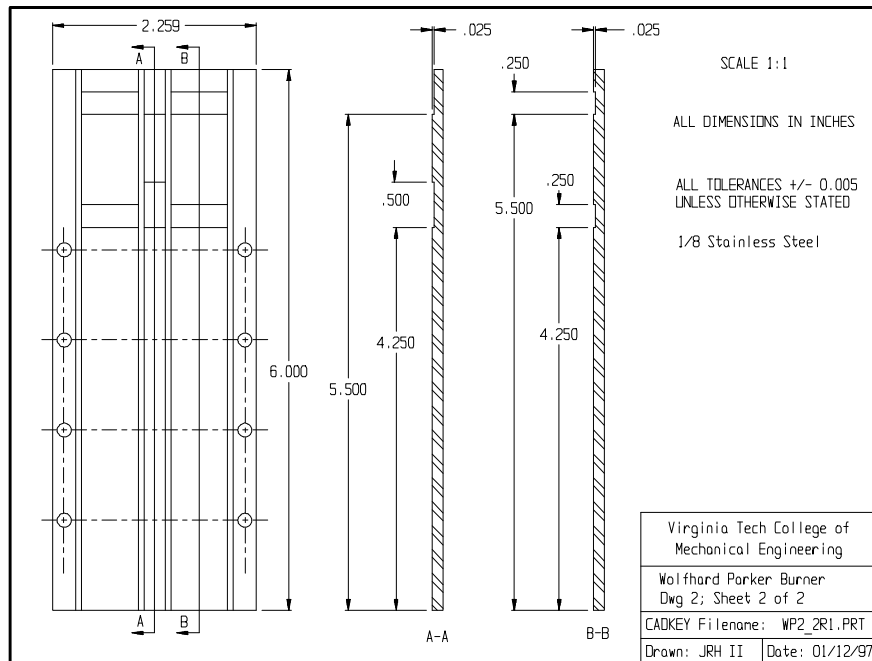


Figure B2 Burner North and South Walls, Drawing 2 Sheet 2 of 2

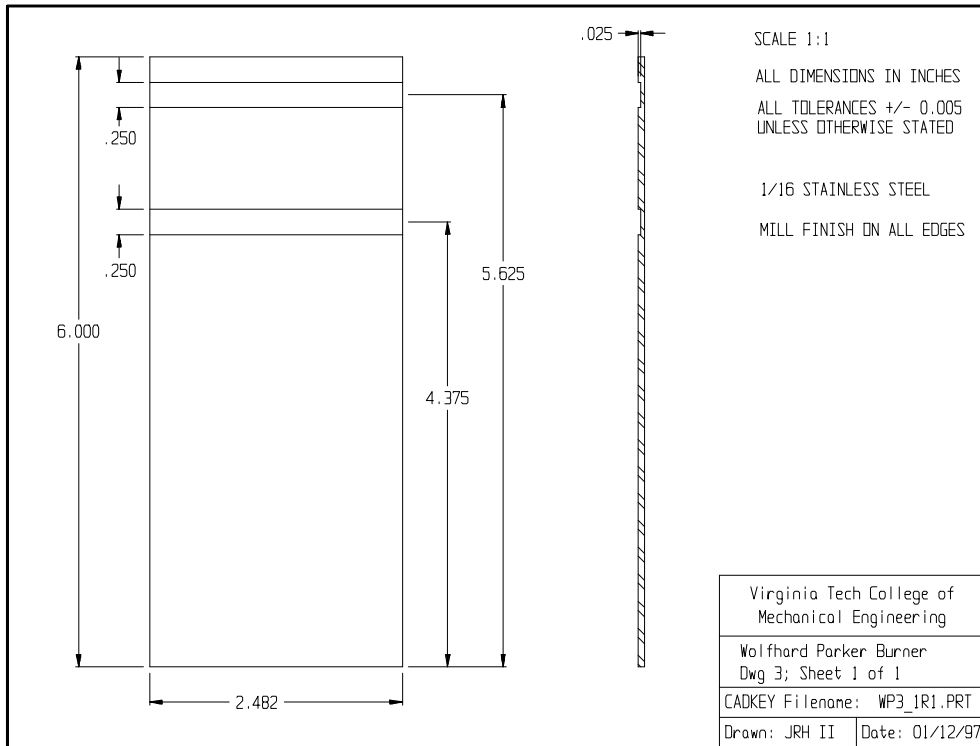


Figure B3 Burner Slot Dividing Walls, Drawing 3 Sheet 1 of 1

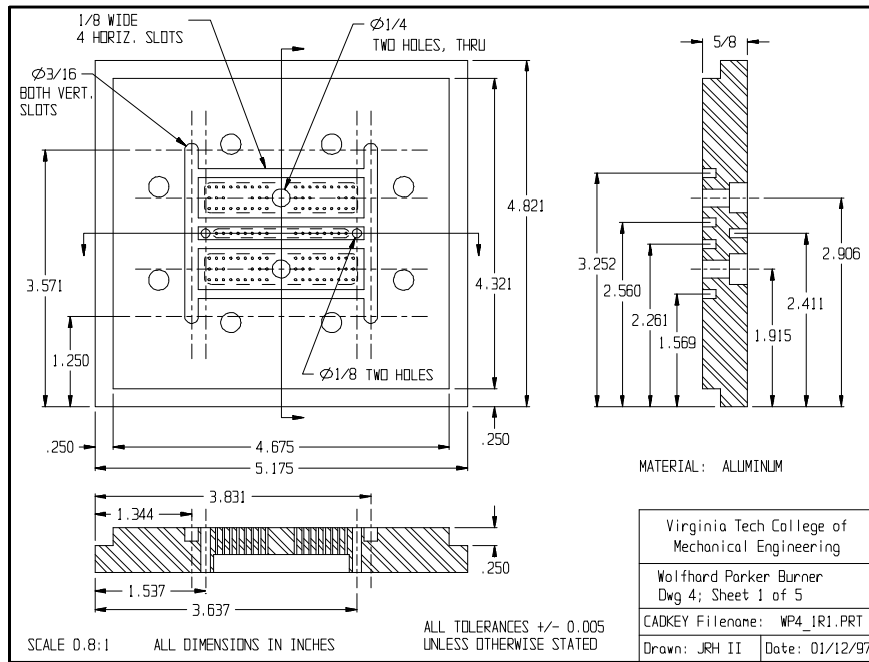


Figure B4 Burner Mounting Base, Drawing 4 Sheet 1 of 5

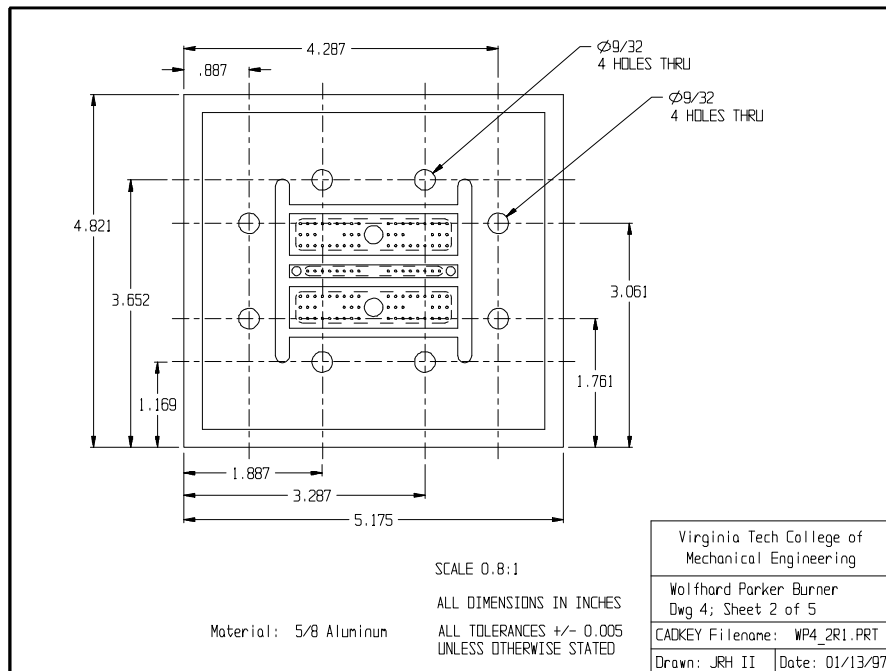


Figure B5 Burner Mounting Base, Drawing 4 Sheet 2 of 5

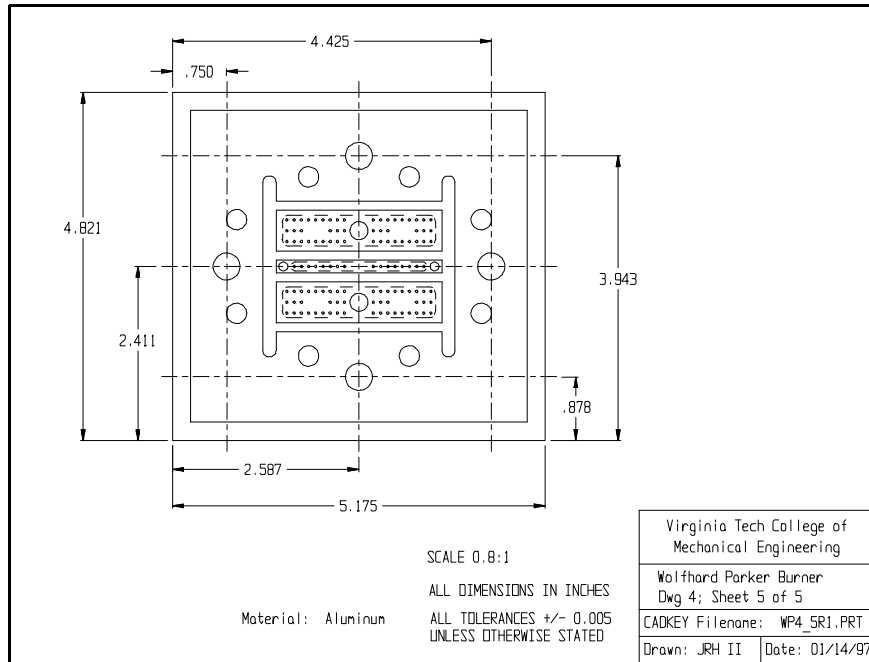


Figure B8 Burner Mounting Base, Drawing 4 Sheet 5 of 5

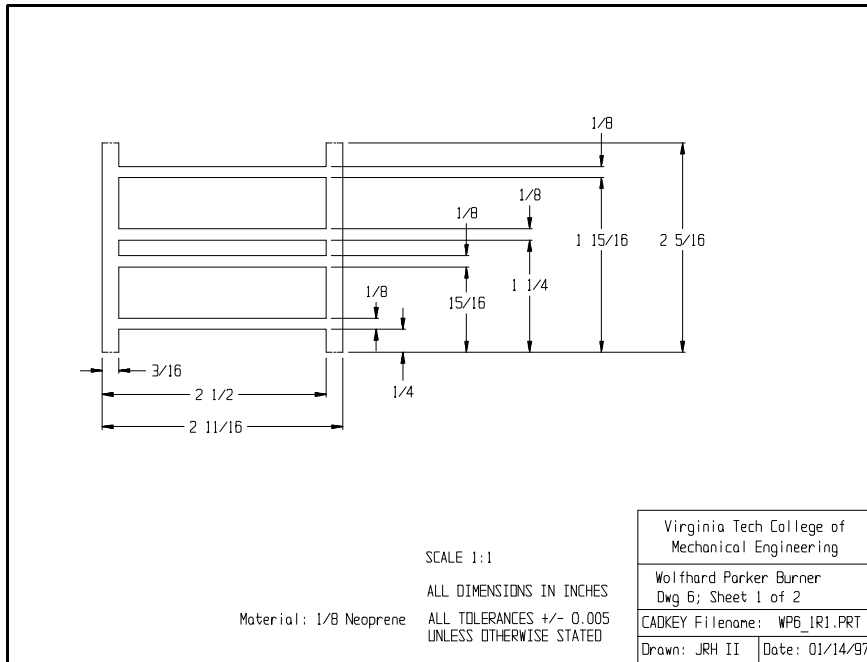


Figure B9 Burner Mounting Base Gasket, Drawing 6 Sheet 1 of 2

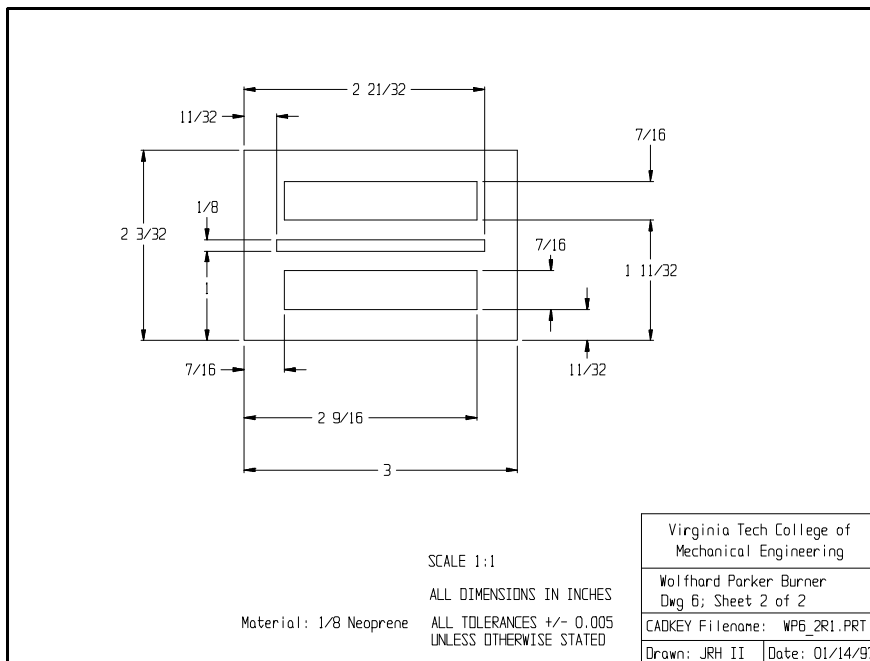


Figure B10 Burner Gas Inlet Manifold Gasket, Drawing 6 Sheet 2 of 2

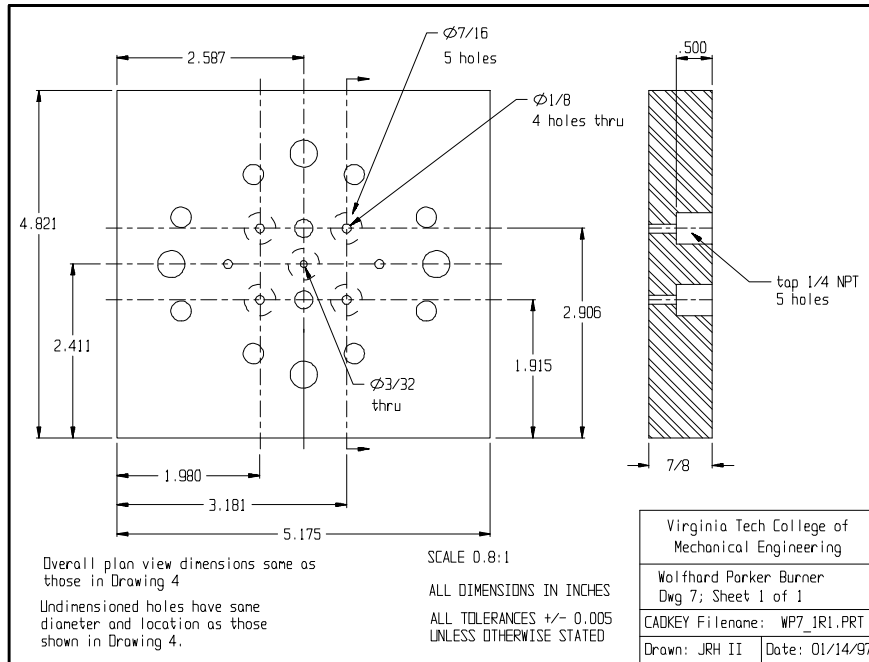


Figure B11 Burner Gas Inlet Manifold, Drawing 7 Sheet 1 of 1

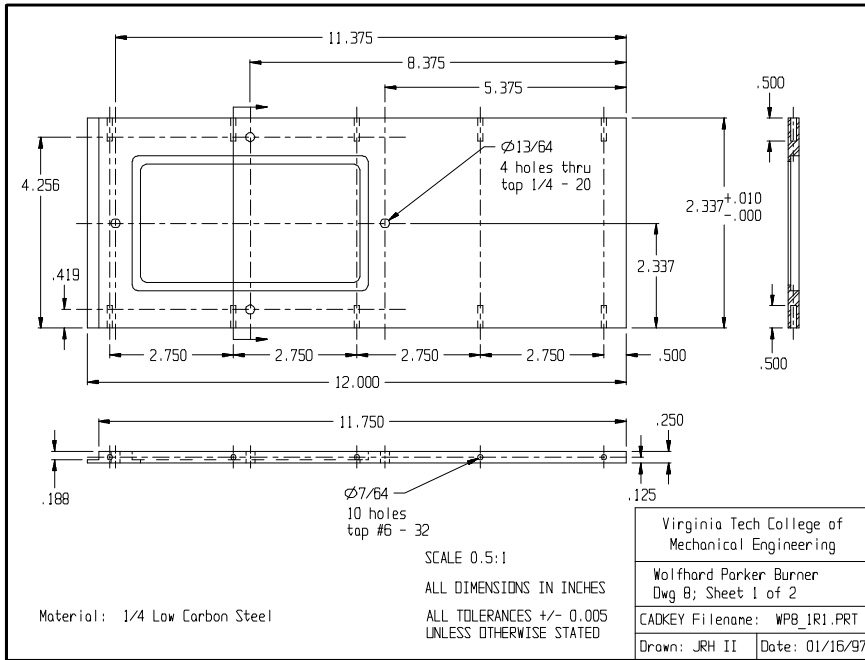


Figure B12 Burner Surround East and West Walls, Drawing 8 Sheet 1 of 2

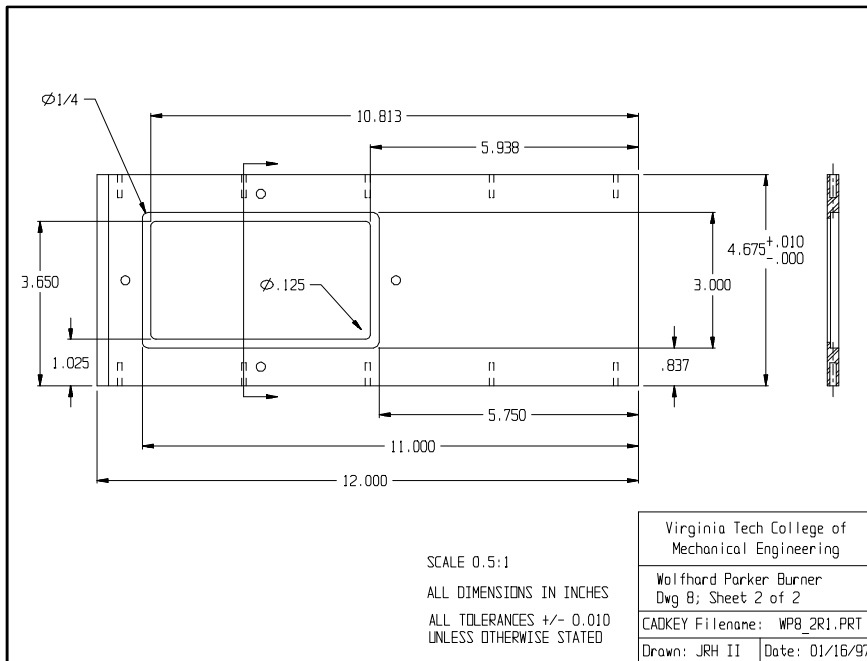


Figure B13 Burner Surround East and West Walls, Drawing 8 Sheet 2 of 2

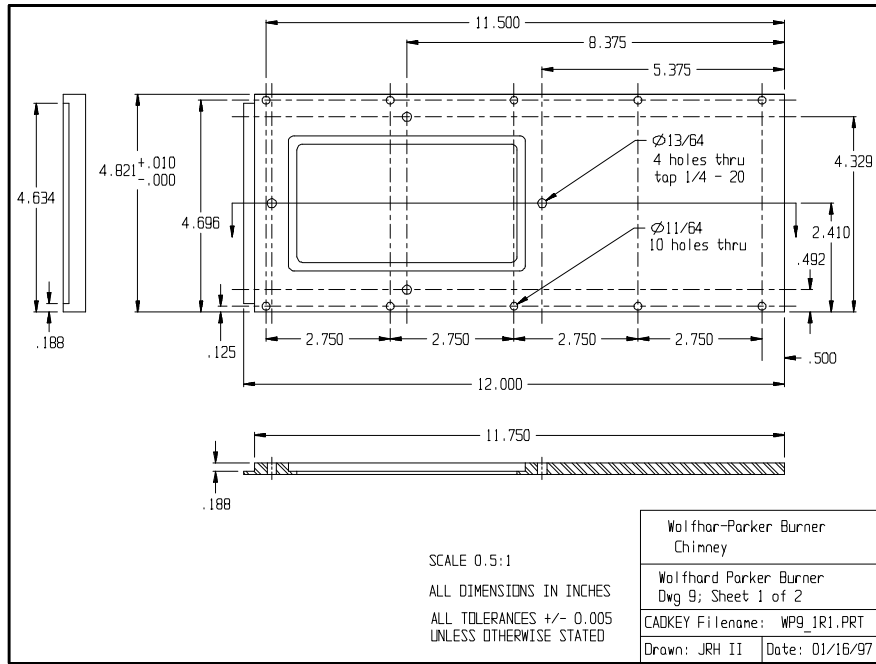


Figure B14 Burner Surround North and South Walls, Drawing 9 Sheet 1 of 2

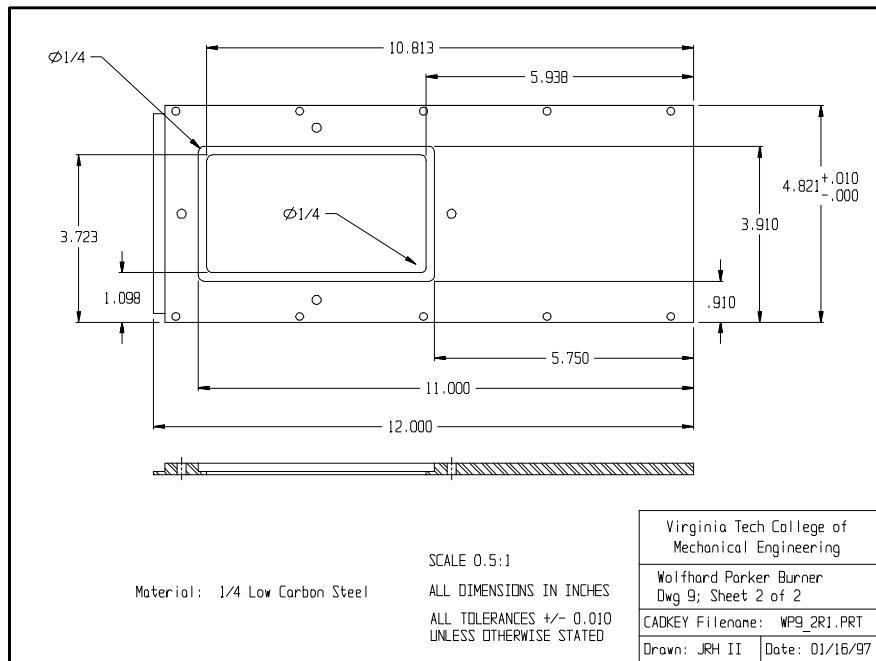
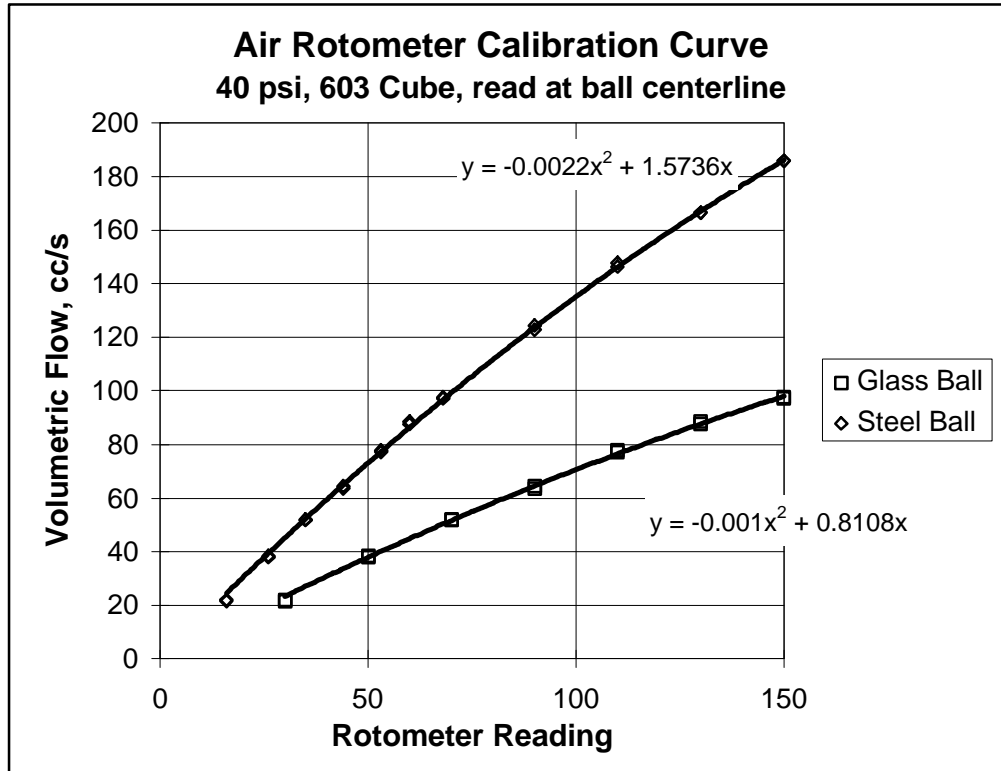


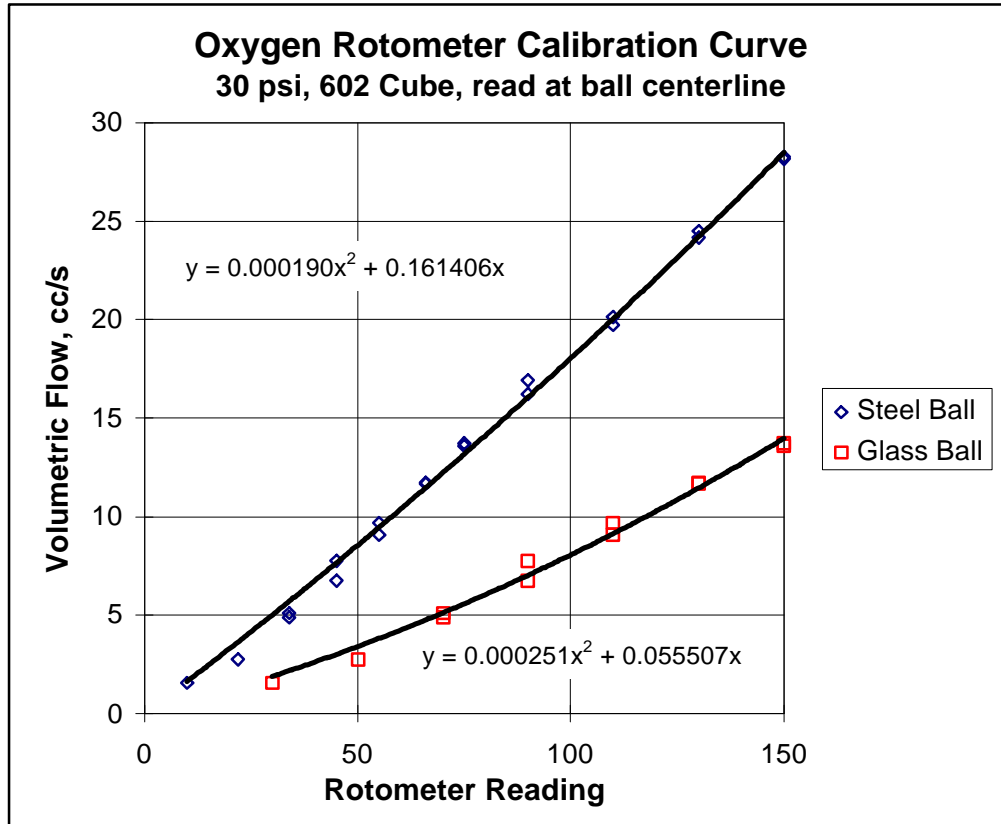
Figure B15 Burner Surround North and South Walls, Drawing 9 Sheet 2 of 2

Appendix C Rotameter Calibrations



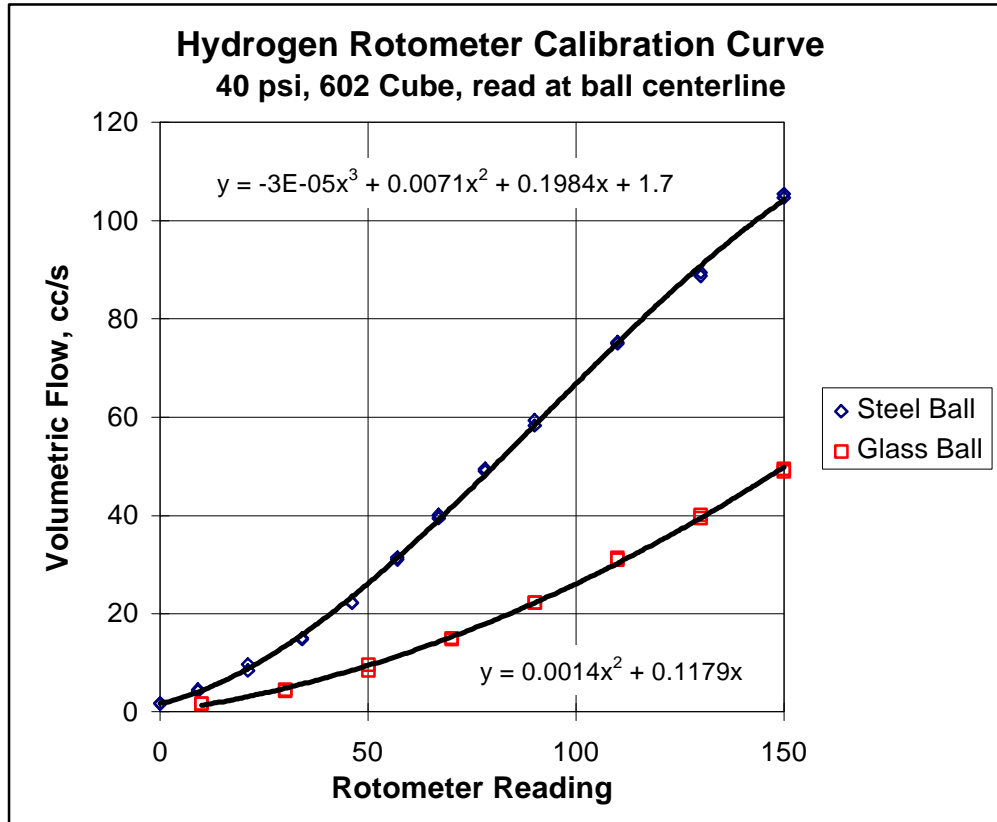
Rotometer Reading	Glass Volume Flow, cc/s	Steel Volume Flow, cc/s	Rotometer Reading	Glass Volume Flow, cc/s	Steel Volume Flow, cc/s
0	0.000	0.000	80	58.464	111.808
5	4.029	7.813	85	61.693	117.861
10	8.008	15.516	90	64.872	123.804
15	11.937	23.109	95	68.001	129.637
20	15.816	30.592	100	71.080	135.360
25	19.645	37.965	105	74.109	140.973
30	23.424	45.228	110	77.088	146.476
35	27.153	52.381	115	80.017	151.869
40	30.832	59.424	120	82.896	157.152
45	34.461	66.357	125	85.725	162.325
50	38.040	73.180	130	88.504	167.388
55	41.569	79.893	135	91.233	172.341
60	45.048	86.496	140	93.912	177.184
65	48.477	92.989	145	96.541	181.917
70	51.856	99.372	150	99.120	186.540
75	55.185	105.645			

Figure C1 Air Rotameter Calibration Curve



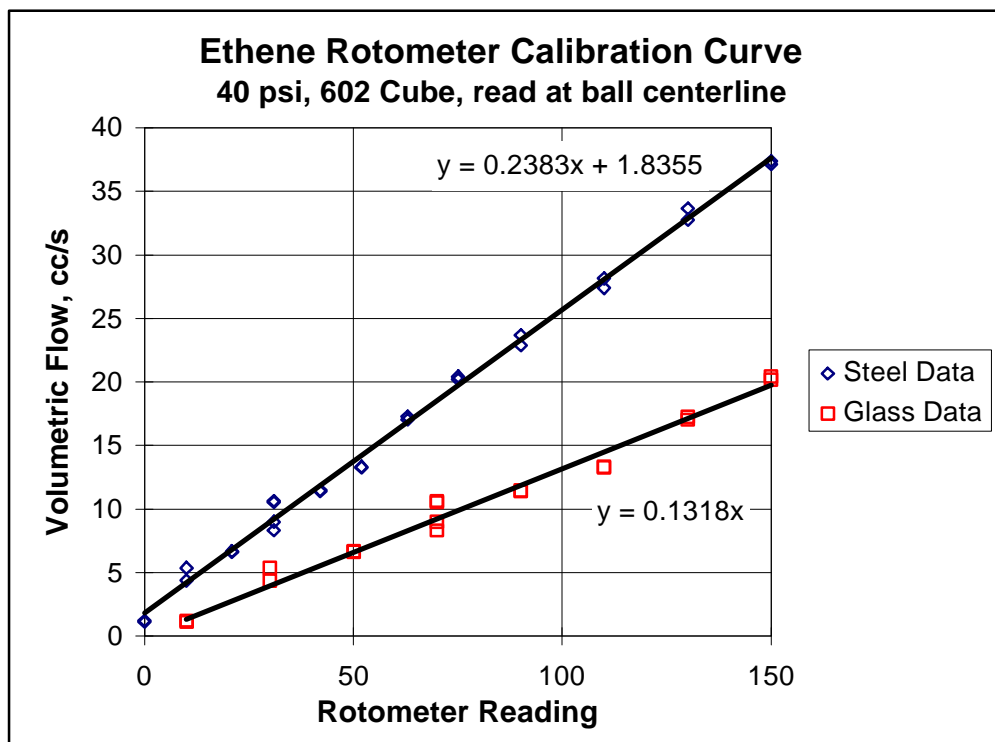
Rotometer Reading	Glass Volume Flow, cc/s	Steel Volume Flow, cc/s	Rotometer Reading	Glass Volume Flow, cc/s	Steel Volume Flow, cc/s
0	0.000	0.000	80	6.047	14.128
5	0.284	0.812	85	6.532	15.092
10	0.580	1.633	90	7.029	16.066
15	0.889	2.464	95	7.538	17.048
20	1.211	3.304	100	8.061	18.041
25	1.545	4.154	105	8.596	19.042
30	1.891	5.013	110	9.143	20.054
35	2.250	5.882	115	9.703	21.074
40	2.622	6.760	120	10.275	22.105
45	3.006	7.648	125	10.860	23.145
50	3.403	8.545	130	11.458	24.194
55	3.812	9.452	135	12.068	25.253
60	4.234	10.368	140	12.691	26.321
65	4.668	11.294	145	13.326	27.399
70	5.115	12.229	150	13.974	28.486
75	5.575	13.174			

Figure C2 Oxygen Rotameter Calibration Curve



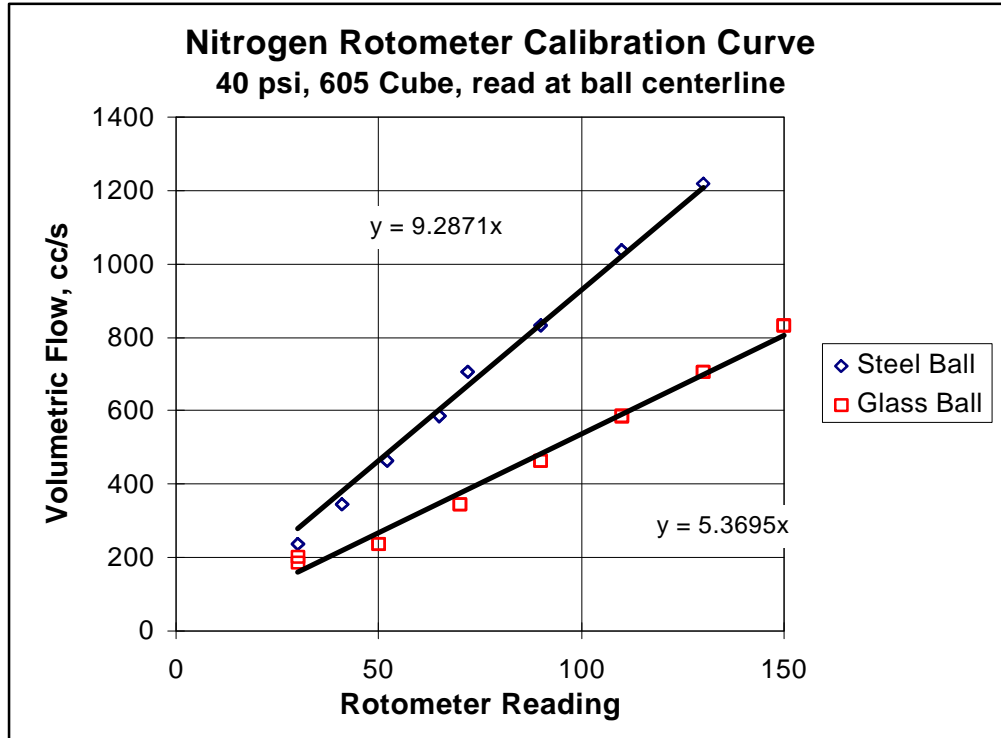
Rotometer Reading	Glass Volume Flow, cc/s	Steel Volume Flow, cc/s	Rotometer Reading	Glass Volume Flow, cc/s	Steel Volume Flow, cc/s
0	0.000	1.700	80	18.392	49.806
5	0.625	2.867	85	20.137	54.014
10	1.319	4.370	90	21.951	58.246
15	2.084	6.190	95	23.836	62.483
20	2.918	8.307	100	25.790	66.705
25	3.823	10.702	105	27.815	70.893
30	4.797	13.356	110	29.909	75.027
35	5.842	16.248	115	32.074	79.088
40	6.956	19.359	120	34.308	83.056
45	8.141	22.671	125	36.613	86.912
50	9.395	26.162	130	38.987	90.637
55	10.720	29.815	135	41.432	94.210
60	12.114	33.608	140	43.946	97.612
65	13.579	37.524	145	46.531	100.824
70	15.113	41.542	150	49.185	103.827
75	16.718	45.642			

Figure C3 Hydrogen Rotameter Calibration Curve



Rotameter Reading	Glass Volume Flow, cc/s	Steel Volume Flow, cc/s	Rotameter Reading	Glass Volume Flow, cc/s	Steel Volume Flow, cc/s
0	0.000	1.836	80	10.544	20.900
5	0.659	3.027	85	11.203	22.091
10	1.318	4.219	90	11.862	23.283
15	1.977	5.410	95	12.521	24.474
20	2.636	6.602	100	13.180	25.666
25	3.295	7.793	105	13.839	26.857
30	3.954	8.985	110	14.498	28.049
35	4.613	10.176	115	15.157	29.240
40	5.272	11.368	120	15.816	30.432
45	5.931	12.559	125	16.475	31.623
50	6.590	13.751	130	17.134	32.815
55	7.249	14.942	135	17.793	34.006
60	7.908	16.134	140	18.452	35.198
65	8.567	17.325	145	19.111	36.389
70	9.226	18.517	150	19.770	37.581
75	9.885	19.708			

Figure C4 Ethylene Rotameter Calibration Curve



Rotometer Reading	Glass Volume Flow, cc/s	Steel Volume Flow, cc/s	Rotometer Reading	Glass Volume Flow, cc/s	Steel Volume Flow, cc/s
0	0.000	0.000	80	429.560	742.968
5	26.848	46.436	85	456.408	789.404
10	53.695	92.871	90	483.255	835.839
15	80.543	139.307	95	510.103	882.275
20	107.390	185.742	100	536.950	928.710
25	134.238	232.178	105	563.798	975.146
30	161.085	278.613	110	590.645	1021.581
35	187.933	325.049	115	617.493	1068.017
40	214.780	371.484	120	644.340	1114.452
45	241.628	417.920	125	671.188	1160.888
50	268.475	464.355	130	698.035	1207.323
55	295.323	510.791	135	724.883	1253.759
60	322.170	557.226	140	751.730	1300.194
65	349.018	603.662	145	778.578	1346.630
70	375.865	650.097	150	805.425	1393.065
75	402.713	696.533			

Figure C5 Nitrogen Rotameter Calibration Curve

Appendix D Uncertainty Analysis

D.1 Measurement Uncertainty

All measurements include some degree of error. The uncertainty associated with experimental data can be quantified by statistically bounding the most probable magnitudes of the measurement error. Placing meaningful bounds on the measurement errors first requires identifying the possible sources of error. When performing measurements on samples representative of some population, bias errors are those which only affect the average of the measurements, \bar{x} , and random errors are those which only affect the standard deviation, S_x , where

$$\bar{x} = \sum_{i=1}^n \frac{x_i}{n} \quad \text{Equation D.1}$$

$$S_x = \sqrt{\frac{\sum_{i=1}^n (x_i - \bar{x})^2}{n - 1}} \quad \text{Equation D.2}$$

where x_i = measurement of i^{th} sample

n = total number of samples

For random errors with a Gaussian distribution, the uncertainty, U_x , that the average of a sample equals the true mean of the population can be related to some constant times the

standard deviation with a finite level of confidence or probability. For instance, with 95% confidence the uncertainty associated with some Gaussian distribution of error can be calculated as

$$U_x = 1.96 \cdot S_x \approx 2.0 \cdot S_x \quad \text{Equation D.3}$$

often approximated as exactly twice the standard deviation.

The uncertainties associated with inputs to a calculation must be propagated through the calculation to quantify the overall uncertainty of the result. Error propagation through calculations is usually performed under the assumption that the uncertainties vary linearly with magnitudes of their corresponding mean values. Consider the dependent variable y which is some function of many independent variables, x_i ,

$$y = f(x_1, x_2, x_3, \dots, x_n)$$

the uncertainty in the value of y , U_y , is typically calculated by linearly propagating the uncertainties of the independent variables, U_{x_i} , through the calculation as

$$U_y = \sqrt{\left(\frac{\partial y}{\partial x_1} U_{x_1}\right)^2 + \left(\frac{\partial y}{\partial x_2} U_{x_2}\right)^2 + \dots + \left(\frac{\partial y}{\partial x_n} U_{x_n}\right)^2} = g(y, x_i) \quad \text{Equation D.4}$$

The remainder of this appendix describes the propagation of random errors through the calculations for thermocouple convection properties (Appendix A Section 5), gas temperatures (Appendix A) and optical extinction soot volume fractions (Chapter 3 Section 5.3).

D.2 Thermocouple Convection Properties Uncertainty

The normalized thermocouple Nusselt number ratio, η , is calculated from Equation A.23 as

$$\eta = \frac{Nu_{sph} - Nu_{rel}}{Nu_{sph} - Nu_{cyl}} \quad \text{Equation A.23}$$

From Equation D.4 the uncertainty in η was calculated as

$$U_{\eta} = g(Nu_{sph}, U_{Nu,sph}, Nu_{rel}, U_{Nu,rel}, Nu_{cyl}, U_{Nu,cyl}) \quad \text{Equation D.5}$$

where

$$\frac{\partial \eta}{\partial Nu_{sph}} = \frac{-(Nu_{sph} - Nu_{rel})}{(Nu_{sph} - Nu_{cyl})^2} + \frac{1}{Nu_{sph} - Nu_{cyl}} \quad \text{Equation D.6}$$

$$\frac{\partial \eta}{\partial Nu_{rel}} = \frac{-1}{Nu_{sph} - Nu_{cyl}} \quad \text{Equation D.7}$$

$$\frac{\partial \eta}{\partial Nu_{cyl}} = \frac{Nu_{sph} - Nu_{rel}}{(Nu_{sph} - Nu_{cyl})^2} \quad \text{Equation D.8}$$

Uncertainty in the Nusselt number empirical relation for flow over spheres was reported by Vliet and Leppert [1961] as $\pm 5\%$. Uncertainty in the Nusselt number empirical relation for flow over infinite cylinders was reported by Colis and Williams [1959] as $\sim 5\%$. To account for uncertainty in the thermocouple junction Reynolds number (based on diameter) an uncertainty of 20% was used for both the cylindrical and spherical Nusselt number relations.

Uncertainty in the measured Nusselt number, Nu_{rel} , was calculated by propagating contributing errors through Equation A.11 according to Equation D.4

$$Nu_{rel} = \frac{\sigma \varepsilon (T_s^4 - T_{sur}^4)}{(T_{gas} - T_s)} \frac{d}{k} \quad \text{Equation A.11}$$

$$U_{Nu,rel} = g(\varepsilon, U_\varepsilon, d, U_d, k, U_k, T_g, U_{Tg}, T_s, U_{Ts}) \quad \text{Equation D.9}$$

where

$$\frac{\partial Nu_{rel}}{\partial \varepsilon} = \frac{\sigma d}{k} \frac{(T_s^4 - T_{sur}^4)}{T_g - T_s} \quad \text{Equation D.10}$$

Thermocouple emissivity, ε , uncertainty reported by Bradley and Entwistle [1961] of $\pm 1.5\%$ was used.

$$\frac{\partial Nu_{rel}}{\partial d} = \frac{\sigma \varepsilon}{k} \frac{(T_s^4 - T_{sur}^4)}{T_g - T_s} \quad \text{Equation D.11}$$

Thermocouple junction diameters, d , were measured under a low power microscope using a scale with a precision of $5 \mu\text{m}$ so an uncertainty of $10 \mu\text{m}$ was used in the calculations.

$$\frac{\partial Nu_{rel}}{\partial k} = \frac{-\sigma \varepsilon}{k^2} \frac{(T_s^4 - T_{sur}^4)}{T_g - T_s} \quad \text{Equation D.12}$$

Since the gas thermal conductivity, k , was assumed to be strictly a function of temperature uncertainty in the gas thermal conductivity was approximated as,

$$U_k = \left(\frac{\partial k}{\partial T_s} \right) \cdot U_{Ts} \quad \text{Equation D.13}$$

$$\frac{\partial Nu_{rel}}{\partial T_s} = \frac{\sigma \varepsilon d}{k} \left[\frac{-(T_s^4 - T_{sur}^4)}{(T_g - T_s)^2} + \frac{4T_s^3}{T_g - T_s} \right] \quad \text{Equation D.14}$$

Standard deviations of ± 3 K in the measured thermocouple surface temperatures, T_s , were typical and a value of 7 K was used as the surface temperature uncertainty.

$$\frac{\partial \text{Nu}_{\text{rel}}}{\partial T_g} = \frac{\sigma \varepsilon d}{k} \frac{(T_s^4 - T_{\text{sur}}^4)}{(T_g - T_s)^2} \quad \text{Equation D.15}$$

Uncertainty in the gas temperature, T_g , was calculated by propagating contributing uncertainties through Equation A.11 according to Equation D.4 as shown in Equation D.16. Recall that the gas temperature is based on the spherical “reference” thermocouple junction (Figure A.8). No attempt was made in this analysis to quantify the uncertainty in the assumed spherical convective properties of the reference junction.

$$T_g = T_s + \sigma \varepsilon (T_s^4 - T_{\text{surr}}^4) \frac{d}{\overline{\text{Nu}}_d \cdot k} \quad \text{Equation A.11}$$

$$U_{T_g} = g(T_s, U_{T_s}, \varepsilon, U_\varepsilon, d, U_d, \text{Nu}_{\text{sph}}, U_{\text{Nu}_{\text{sph}}}, k, U_k) \quad \text{Equation D.16}$$

$$\frac{\partial T_g}{\partial T_s} = \frac{4\sigma \varepsilon d}{\text{Nu}_{\text{sph}} k} T_s^3 \quad \text{Equation D.17}$$

$$\frac{\partial T_g}{\partial \varepsilon} = \frac{\sigma d}{\text{Nu}_{\text{sph}} k} (T_s^4 - T_{\text{sur}}^4) \quad \text{Equation D.18}$$

$$\frac{\partial T_g}{\partial d} = \frac{\sigma \varepsilon}{\text{Nu}_{\text{sph}} k} (T_s^4 - T_{\text{sur}}^4) \quad \text{Equation D.19}$$

$$\frac{\partial T_g}{\partial \text{Nu}_{\text{sph}}} = \frac{-\sigma \varepsilon d}{\text{Nu}_{\text{sph}}^2 k} (T_s^4 - T_{\text{sur}}^4) \quad \text{Equation D.20}$$

$$\frac{\partial T_g}{\partial k} = \frac{-\sigma \varepsilon d}{\text{Nu}_{\text{sph}} k^2} (T_s^4 - T_{\text{sur}}^4) \quad \text{Equation D.21}$$

D.3 Gas Temperature Uncertainty

Uncertainty in the gas temperatures, T_g , measured in the Wolfhard-Parker flames were calculated by propagating contributing uncertainties through Equation A.11 according to Equation D.4 as shown in Equation D.22.

$$T_g = T_s + \sigma \varepsilon (T_s^4 - T_{\text{surr}}^4) \frac{d}{\overline{Nu}_d \cdot k} \quad \text{Equation A.11}$$

$$U_{T_g} = g(T_s, U_{T_s}, \varepsilon, U_\varepsilon, d, U_d, Nu, U_{Nu}, k, U_k) \quad \text{Equation D.22}$$

Notice that the form of Equation D.22 is identical to that in Equation D.16 except that a “typical” thermocouple was used instead of the reference spherical junction during the Wolfhard-Parker flame temperature measurements. The difference in Nusselt numbers does not change the general form of the derivatives, Equations D.16 - D.20, necessary to evaluate Equation D.21. Uncertainties in the thermocouple junction diameters were 10 μm and uncertainties in the gas thermal conductivity were calculated according to Equation D.13. Similar to the thermal conductivity uncertainty calculation the uncertainty in temperature was propagated through the thermocouple emissivity according to Equation D.23 below.

$$U_\varepsilon = \left(\partial \varepsilon / \partial T_s \right) \cdot U_{T_s} + 0.03 \cdot \varepsilon \quad \text{Equation D.23}$$

Uncertainties in the measured thermocouple surface temperatures, T_s , were calculated based the ANSI standard MC 96.1 [1975] of $\pm 0.5\%$. Standard deviation calculated in nonsooting regions of the flame typically had standard deviations on the order of 1 K. No attempt was made in this analysis to quantify errors specific to the rapid insertion technique.

The results from Appendix A, Section 5 were used to quantify the convection properties of the thermocouples used. Thermocouple junction diameters were approximately $100 \pm 15 \mu\text{m}$ yielding junction diameter to wire diameter ratios of 2.0 ± 0.3 . These junctions fall in the upper left hand corner of Figure A.10 indicating primarily cylindrical behavior. From Figure A.10 the normalized Nusselt number ratio, η , was taken as 0.9 with an uncertainty of 0.15. From η the thermocouple junction Nusselt number was calculated from

$$\text{Nu}_{\text{rel}} = \text{Nu}_{\text{sph}} - \eta \cdot (\text{Nu}_{\text{sph}} - \text{Nu}_{\text{cyl}}) \quad \text{Equation A.23}$$

Propagating relevant errors through the calculation according to Equation D.4 yields

$$U_{\text{Nu,rel}} = g(\eta, U_{\eta}, \text{Nu}_{\text{sph}}, U_{\text{Nu,sph}}, \text{Nu}_{\text{cyl}}, U_{\text{Nu,cyl}}) \quad \text{Equation D.24}$$

where

$$\frac{\partial \text{Nu}_{\text{rel}}}{\partial \eta} = -(\text{Nu}_{\text{sph}} - \text{Nu}_{\text{cyl}}) \quad \text{Equation D.25}$$

$$\frac{\partial \text{Nu}_{\text{rel}}}{\partial \text{Nu}_{\text{sph}}} = 1 - \eta \quad \text{Equation D.26}$$

$$\frac{\partial \text{Nu}_{\text{rel}}}{\partial \text{Nu}_{\text{cyl}}} = \eta \quad \text{Equation D.27}$$

Uncertainties used for the empirical Nusselt number relations for spheres and cylinders were 20%, identical to those used in Appendix D, Section 2.

D.4 Extinction Soot Volume Fraction Uncertainty

Propagating errors through Equation 3.2 for the soot volume fraction according to Equation D.4 yields Equation D.28.

$$\phi = \frac{\lambda k_{\text{ext}}}{6\pi \cdot E(\tilde{m})} \quad \text{Equation 3.2}$$

$$U_{\phi} = g(k_{\text{ext}}, U_{k_{\text{ext}}}, E(\tilde{m}), U_{E(\tilde{m})}) \quad \text{Equation D.28}$$

where

$$\frac{\partial \phi}{\partial k_{\text{ext}}} = \frac{\lambda}{6\pi E(\tilde{m})} \quad \text{Equation D.29}$$

$$\frac{\partial \phi}{\partial E(\tilde{m})} = \frac{-\lambda k_{\text{ext}}}{6\pi E(\tilde{m})^2} \quad \text{Equation D.30}$$

Many values for the complex index of refraction of soot, \tilde{m} , are reported in the literature [Smyth and Shaddix, 1996] with no reliable estimates of uncertainty. Uncertainty of $E(\tilde{m})$ was arbitrarily chosen as $\pm 10\%$ for these calculations.

Propagating relevant uncertainties through the calculation for the extinction coefficient, Equation 3.4, according to Equation D.4 yields Equation D.31

$$k_{\text{ext}} = -\frac{1}{L} \ln\left(\frac{I}{I_0}\right) \quad \text{Equation 3.4}$$

$$U_{k_{\text{ext}}} = g(L, U_L, I/I_0, U_{I/I_0}) \quad \text{Equation D.31}$$

$$\frac{\partial k_{\text{ext}}}{\partial L} = \ln\left(\frac{I}{I_0}\right) \frac{1}{L^2} \quad \text{Equation D.32}$$

Extinction path lengths, L, were measured with a precision of 1 mm so an uncertainty of 2mm was used to account for extinction path length error on both the incident and transmitting sides of the flame sheets.

$$\frac{\partial k_{\text{ext}}}{\partial \left(\frac{I}{I_0} \right)} = - \left(\frac{I_0}{I} \right) \frac{1}{L} \quad \text{Equation D.33}$$

where

$$U_{I/I_0} = \sqrt{\left(\frac{1}{I_0} \cdot 2S_I \right)^2 + \left(\frac{I}{I_0^2} \cdot 2S_{I_0} \right)^2} \quad \text{Equation D.34}$$

Equation D.3 was used to estimate uncertainties in the incident and transmitted laser light as twice the standard deviation of the time averaged signals.

Vita

Joell R. Hibshman II (Randy) was born November 24, 1972 in West Point, New York. He graduated from Nottoway High School in Nottoway, Virginia in the Spring of 1990. Randy embarked on a marathon collegiate career at Virginia Polytechnic Institute and State University in Blacksburg, Virginia in the Fall of 1990. After nine semesters of classes intermingled with five cooperative education work sessions at Virginia Power's Possum Point Power Station, Randy received his Bachelor of Science degree in Mechanical Engineering, Magna Cum Laude, in December of 1995. He enrolled in a Master of Science graduate program in Virginia Tech's Reacting Flows Laboratory in January of 1996. Randy currently lives in Vernon, Connecticut and works as an Assistant Research Engineer in the Combustion Technology Group at United Technologies Research Center.

Joell R. Hibshman II